A general formulation for cavitating, boiling and evaporating flows

Richard Saurel[1a,c,d], Pierre Boivin[c], Olivier Le Métayer[b]

[a] *University Institute of France*
[b] *Aix-Marseille University, CNRS IUSTI, 5 rue E. Fermi, 13453 Marseille, France*
[c] *Aix-Marseille University, CNRS M2P2, 38 rue J. Curie, 13451 Marseille, France*
[d] *RS2N, Chemin de Gaumin, 83640 Saint-Zacharie, France*

Abstract

A flow model is derived for the numerical simulation of multi-phase flows with phase transition. The model arises from the classical multi-component Euler equations, but is associated to a non-classical thermodynamic closure: each phase is compressible and evolves in its own subvolume, with phases sharing common pressure, velocity and temperature, leading to non-trivial thermodynamic relations for the mixture. Phase transition is made possible through the introduction of Gibbs free energy relaxation terms in the equations. Capillary effects and heat conduction – essential in boiling flows – are introduced as well.

The resulting multi-phase flow model is hyperbolic, valid for arbitrary density jumps at interfaces as well as arbitrary flow speeds. Its capabilities are illustrated successively through examples of nozzle induced cavitation, a high-speed evaporating liquid jet, and heated wall induced boiling.

Keywords: multiphase flows, interfaces, hyperbolic systems, relaxation, phase transition.

[1]Corresponding author: `richard.saurel@univ-amu.fr`

1. Introduction

Cavitating, boiling and evaporating are three phenomena that involve phase transition in multiphase flows. They appear in countless engineering applications: steam generators, marine propellers, liquid fuel combustion, etc. Yet, modelling these phenomena remains an unsettled problem.

Cavitation in a liquid is a phase change phenomenon created by a pressure drop driven by (fast) acoustic waves, generating - as its name suggests - gas cavities. When pressure becomes lower that the saturation one at the local temperature, phase change appears as the liquid internal energy or temperature is greater than the saturated one: the liquid is overheated. Indeed, during a pressure drop, the liquid temperature varies weakly and at low pressure it becomes hot compared to the saturation temperature, this one being strongly dependant of pressure.

Boiling is yet another phase transition phenomenon created by heat deposition in a liquid, most times by heat conduction from a hot wall. The heating increases the liquid temperature and when it becomes greater than the saturation temperature at local pressure (most times uniform in the domain) phase change appears. Therefore, unlike cavitation, this process is governed by (slow) heat conduction.

In both instances, the liquid is overheated due to a departure from the saturation conditions, whether it comes from a pressure drop (cavitation) or from a temperature rise (boiling). Consequently, phase change occurs, provided that some impurities (nucleation sites) are present. In industrial and natural fluids impurities are always present in large enough concentrations

(solute gases, trapped bubbles in wall roughness etc.).

Evaporation differs from boiling in that the liquid is not necessarily at its boiling temperature, but phase transition occurs nonetheless at its surface because of heat and mass fluxes at the liquid/gas interface. At the interface, local thermodynamic equilibrium implies the presence of liquid vapor in the gas mixture, with a partial pressure equal to the saturating pressure at the interface temperature.

To summarize, all of these processes occur due to a local balancing of Gibbs free energies between the liquid, and the vapor or gas mixture. Cavitation is oftentimes assumed to be isothermal, with severe pressure gradients, whereas boiling and evaporation are roughly isobaric, with important temperature gradients (Sinibaldi *et al.* 2006, d'Agostino and Salvetti 2008, Goncalves and Patella 2009). Although they have different characteristic times, as pressure gradients are associated to acoustic waves (fast), and temperature gradients to heat conduction (slow), cavitation, boiling and evaporation are driven by phase transition and may therefore be modelled by the same approach.

However, in the literature, cavitation, boiling and evaporating flows are considered through very different approaches. Most cavitation models consider liquid and two-phase mixture evolving at uniform temperature (Coutier-Delgosha *et al.* 2003, Barre *et al.* 2009). In these formulations the flow model is barotropic and the energy conservation principle as well as the second law of thermodynamics are omitted. In these models, the EOS is built to mimic some behaviour of two-phase mixtures, such as the mixture sound speed that evolves non-monotonically with respect to the volume fraction. Other cavi-

tation models consider non-isothermal governed by three and four equations models, namely "Homogeneous Equilibrium Models" (HEM) and "Homogeneous Relaxation Model" (HRM), as in Downar-Zapolski *et al.* (1996) and Barret *et al.* (2002).

Boiling flows are considered by different approaches, most of them being based on Cahn and Hilliard (1958) approach of capillary fluids. Here the energy equation is considered as the importance of energetic effects are obvious. Contrarily to cavitation models, sound propagation is wrongly considered, as the square sound speed may become negative in the phase change domain (Menikoff and Plohr 1989). Indeed, the EOS is of cubic-type (van der Waals for example), with undefined sound speed in specific thermodynamic domain. Many other restrictions appear with the Cahn-Hilliard second gradient theory, such as for example the need to enlarge interfaces to make possible practical computations (Jamet *et al.* 2001). Fundamental issues also arise, such as shock wave existence in these media. The two most popular approaches for cavitating and boiling flows have consequently obvious limitations and restrictions.

In the present work a unified approach is provided and its ability to model and compute cavitating, boiling and evaporating flows is shown with computational examples. Most of the scientific material results of former investigations by Saurel *et al.* (2008), Le Martelot *et al.* (2013, 2014). The flow model is a hyperbolic system of partial differential equations with Gibbs free energy relaxation. The thermodynamic closure is built without ambiguity and results in a mixture EOS valid in pure liquid, pure vapour and two-phase mixture. The presence of non-condensable phase may be consid-

ered as well. The sound speed is defined in all space of variables. Non-linear waves, such as shocks have a clear definition too. Last, the formulation is valid for any flow speed and any fluid density ratio at interfaces.

2. Basic flow model specification

The flow model has to deal with:

a) Liquid and gas compressibility: liquid compressibility consideration is mandatory in cavitating flows and gas compressibility must be addressed in most situations of flows with phase change.
b) Pure liquid and pure gas dynamics as well as interfaces motions.
c) Mass exchange in mixtures and at interfaces, for both evaporation and condensation.
d) Heat conduction, important in boiling flows.
e) Capillary effects, important in boiling flows as well.

Obviously the flow model has to be in agreement with the basic principles of physics such as mass, momentum and energy conservation, second law of thermodynamics, frame invariance and thermodynamic consistency (convexity of the EOS and sound speed existence) resulting in hyperbolicity. In the basic flow model version we address items a) and b) that are the most challenging. The model we address considers mixtures and material interfaces in:

– velocity and pressure equilibrium (mechanical equilibrium),

– temperature equilibrium (thermal equilibrium).

This set of constraints is obviously valid in pure phases. In two-phase mixtures it assumes that velocity slip is absent and that the mixing is fine enough to reach temperature equilibrium. It means that the two-phase mixture is made of small drops, small bubbles or foams. Experimental observations of cavitating and flashing flows near macroscopic interfaces support these assumptions (Simoes-Moreira and Shepherd 1999). From these assumptions it is possible to reduce non-equilibrium two-phase flow models to mechanical and thermal equilibrium one. Such reduction method is addressed in Kapila *et al.* (2001), Murrone and Guillard (2005), Saurel *et al.* (2008), Lund (2012), Le Martelot *et al.* (2014) to cite a few. It results in the following system of partial differential equations:

$$
\begin{aligned}
&\frac{\partial(\alpha\rho)_1}{\partial t} + div\big((\alpha\rho)_1\mathbf{u}\big) = 0, \quad \text{or alternatively} \quad \frac{\partial\rho}{\partial t} + div(\rho\mathbf{u}) = 0\\
&\frac{\partial(\alpha\rho)_2}{\partial t} + div\big((\alpha\rho)_2\mathbf{u}\big) = 0 \qquad\qquad \frac{\partial\rho Y_1}{\partial t} + div(\rho Y_1\mathbf{u}) = 0\\
&\frac{\partial\rho\mathbf{u}}{\partial t} + div\left(\rho\mathbf{u}\otimes\mathbf{u} + p\underline{\underline{I}}\right) = 0\\
&\frac{\partial\rho E}{\partial t} + div\left((\rho E + p)\mathbf{u}\right) = 0
\end{aligned}
\tag{1}
$$

Where α_k, Y_k, ρ_k (k=1,2) denote respectively the volume fraction, the mass fraction and the material density. ρ represents the mixture density ($\rho = \alpha_1\rho_1 + \alpha_2\rho_2$), u represents the centre of mass velocity, p denotes the pressure and E the mixture total energy ($E = e + u^2/2$). The mixture internal energy is defined as $e = Y_1e_1 + Y_2e_2$.

System 1 is clearly reminiscent of the reactive (or multi-component) Euler equations widely used in chemically reacting flows. However, the thermodynamic closure departs significantly of the one used in gas mixtures. Indeed,

in the present context it results from the following algebraic system:

$$\begin{cases} T_1 = T_2 = T, \\ e = Y_1 e_1(T,p) + Y_2 e_2(T,p), \\ p_1 = p_2 = p, \\ \alpha_1 + \alpha_2 = 1 \text{ or alternatively, } Y_1 v_1(T,p) + Y_2 v_2(T,p) = v \end{cases} \tag{2}$$

In this algebraic system, the phases are in pressure equilibrium and each one occupies its own sub-volume or volume fraction α_k . System 2 corresponds to a non-linear system of two equations with the two unknowns T and p. To determine its explicit solution, EOS for the phases have to be provided. This is addressed in the forthcoming section. This thermodynamic closure differs significantly from that of ideal gas mixtures. In ideal mixtures each fluid occupies the entire volume, this assumption replacing the last equality of System (2). Also, the pressure is defined by the Dalton's law $p = \sum_k p_k$ instead of the pressure equilibrium condition. In formulation (1) with thermodynamic closure (2) each phase occupies its own volume (and not the entire one) and evolves in temperature and pressure equilibrium with the other phase.

At interfaces separating pure liquid and pure gas the assumption of single temperature seems unrealistic as interface conditions, in the absence of mass transfer and heat diffusion, reduce to equal normal velocities and equal pressures, implying arbitrary temperature jumps. However, when heat diffusion is present an additional interface condition appears, corresponding to temperatures equality. Thus System (2) is valid for the computation of interfacial flows when:

– Heat diffusion is present and when it is possible to resolve the heat diffusion layer, as for example in the boiling flow configurations that will be considered latter. This is similar to laminar flames computations.

– A mushy zone is present at the interface. This is the case for example with flashing and super-cavitating flows where the interface is not a clear discontinuity but a sharp mixture layer in which thermodynamic relaxation and heat exchanges occur intensively. This is similar to turbulent flames computations, where it is not possible to resolve all heat diffusion and chemical relaxation layers at subscale, but for which 'turbulent heat conduction' implies global turbulent flame propagation.

System (1) with closure (2) is thus valid for the computation of:

– local interface dynamics when heat transfer is considered (this effect will be inserted later),

– global (or macro-scale) interface dynamics when a micro-scale or sub-scale structure such as a mushy zone is present. Indeed, at subscale, heat transfer is necessarily present, imposing temperature equality at the interface.

When phase transition is addressed Gibbs free energy relaxation terms have to be considered in one of the mass equations:

$$\frac{\partial \rho Y_1}{\partial t} + \frac{\partial \rho u Y_1}{\partial x} = \rho \nu (g_2 - g_1) \tag{3}$$

where $g_k = h_k - T s_k$ denotes the phase k Gibbs free energy. h_k and s_k represent the specific enthalpy and specific entropy. ν represents a relaxation

parameter ($\nu = \nu(A_I, p, T)$ where A_I represents the specific interfacial area) that controls the rate at which thermodynamic equilibrium is reached. The way this relaxation parameter is estimated will be addressed later.

The entropy equation associated to System (1)-(3) reads,

$$\frac{\partial \rho s}{\partial t} + \frac{\partial \rho s u}{\partial x} = \frac{\rho \nu (g_2 - g_1)^2}{T}, \tag{4}$$

with the following definition for the mixture entropy: $s = Y_1 s_1 + Y_2 s_2$.

The formulation given by Eqs. (3-4) assumes mixtures in thermal and kinematic equilibrium, i.e. not too far from thermodynamic equilibrium.

The same type of remark as before with temperature equality at interfaces is needed to explain the validity of a single velocity model to compute interfacial flows with phase transition. When heat diffusion and Gibbs energy relaxation are addressed and solved at the interface, i.e., when the interface structure is solved, three velocities appear at the global scale even if a single local velocity is present in the flow model. The three velocities that appear at the global scale are the liquid one, the vapour one and the phase transition front one.

This is similar to flames computation in which the reactive Navier-Stokes equations are appropriate to compute the reacting and burnt gas dynamics as well as flame front dynamics.

The model has been shown to converge to exact sharp interface solutions in Le Martelot *et al.* (2014). When the interface has more complex structure with turbulent mixing at subscale, the same three velocities appear with different dynamics. This is a consequence of turbulent heat diffusion and effective properties of fluid media. In the limit, when flash evaporation is considered, the front velocity doesn't exceed the acoustic wave speed of

System (1) or its thermodynamic equilibrium analogue when the relaxation parameter ν in Equation (3) tends to infinity. Indeed, metastable liquid is produced at a rate controlled by expansion waves, themselves propagating at the speed of acoustic waves (Saurel *et al.* 2008). In this limit, the deflagration speed of Chapman-Jouguet (Chaves 1984) is recovered as kinetic relation for the global phase change front velocity. To summarize the discussion on the validity of flow model (1), it is unable to compute accurately interfaces of simple mechanical contact but it becomes valid:

- when heat conduction is considered and the interface structure is resolved, as done for boiling flows (Le Martelot *et al.* 2014),
- when phase change occurs through interfaces with subscale structure, such as cavitating and flashing flows (Saurel *et al.* 2008, Le Martelot *et al.* 2013).

For practical use of System (1)-(2), EOSs have to be specified for the various phases. This is the aim of the next section.

3. Equations of State

Phase transition and equations of state is a long lasting challenge.

About the van der Waal EOS

As mentioned in the introduction, the Cahn-Hilliard (1958) approach is quite popular with boiling flows modelling. It uses the van der Waals (VdW) equation of state (EOS) to compute the pressure. This EOS provides the

pressure for the liquid phase, the gas phase and the two-phase mixture. It reads,

$$p = \frac{\rho RT}{1 - \rho b} - c\rho^2 \tag{5}$$

where R denote the specific gas constant ($R = \frac{r}{W}$) with r =8.314 J/mol/K and W (kg/mol) the molar mass. b represents the specific covolume, i.e. the volume occupied by the molecules (m^3/ kg) and c is a constant associated to attractive effects.

This EOS combines three main effects:

- Thermal agitation, present in all states of matter (solid, liquid and gas) and summarized by the term ρRT.
- Repulsive effects, present in condensed matter (solid and liquid) and in dense gases. These effects are summarized in the term $(1 - \rho b)^{-1}$. When the density increases these effects increase too.
- Attractive effects, present in condensed matter only and summarized in the term $-c\rho^2$. When the density is high enough, molecules are close each other and attractive (electro-magnetic molecular) effects appear. These effects are short distance ones and vanish as soon as the molecules are far enough.

The VdW EOS is thus particular attractive as it combines all possible effects occurring in matter. Its particular interest for phase transition modelling relies in the attractive pressure ($-c\rho^2$) that vanishes when the density becomes low.

However this EOS contains a fundamental drawback schematized in Fig. 1 where an isentrope for the VdW EOS is shown. An alternative to cure this

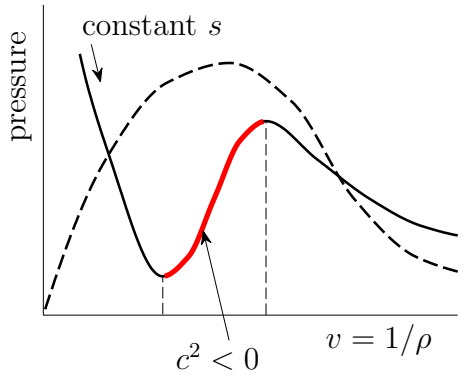

Figure 1: Thermodynamic path along an isentrope showing an expansion process starting from a pure liquid to the pure vapour region. The square sound speed $c^2 = -v^2 \frac{\partial p}{\partial v}\Big)_s$ is well defined in the pure liquid and pure gas but is undefined in the two-phase region, between the metastable liquid and the metastable gas.

deficiency is described in e.g. Wareing *et al.* (2013) with the help of a composite formulation. In this approach, the pure liquid and pure gas phases are governed by a cubic EOS, but the two-phase mixture is computed using the assumption of equality of the pressure, temperature and Gibbs free energies of the phases. More precisely, the temperature is the saturation one at the current pressure and the mixture composition is deduced from mixture specific volume and internal energy definitions (see for example Orbey and Sandler (1998)). A similar method was used in Saurel *et al.* (1999) but a key point of the method of Wareing *et al.* (2013) is precisely the use of cubic EOS for pure phases, instead of crude approximations. A typical transformation with the composite EOS is shown in Fig. 2.

In the following we adopt a method quite close to the one of Wareing *et al.* (2013). Cubic EOS for pure fluids are replaced by simpler approximations (Stiffened Gas and Noble-Abel-Stiffened Gas EOSs) as shown hereafter. Most of the composite formulation of Wareing is now done at the continuous level

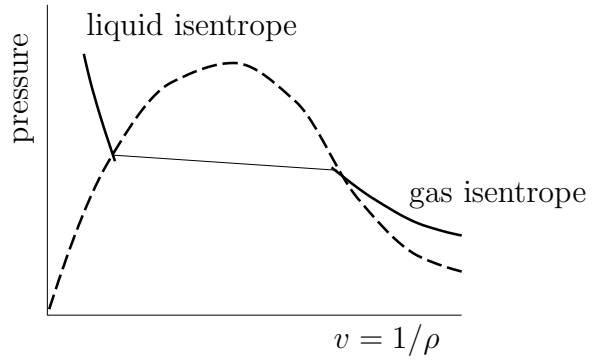

Figure 2: Liquid, gas and two-phase mixture isentrope with the method of Wareing *et al.* (2013).

with the help of the flow model (1) with the thermodynamic closure that follows.

EOS for pure fluids

In the following we adopt an approach where each phase has its own EOS, each EOS being thermodynamically consistent (convex) with well defined sound speed. The connexion between the two phases is done through a kinetic path instead of a thermodynamic one. Determination of the kinetic relaxation rate will be addressed later. Schematic representation of the thermo-kinetic approach of phase transition is shown in Figure 3. This idea was promoted in Saurel *et al.* (2008).

In this frame, liquid and gas require their own EOS, these ones being linked by the phase diagram. The building of such EOS has been addressed in Le Métayer *et al.* (2004) on the basis of the stiffened gas (SG) EOS. An improved formulation is given hereafter, based on Le Métayer and Saurel (2015). It can be considered as an improved stiffened gas formulation or

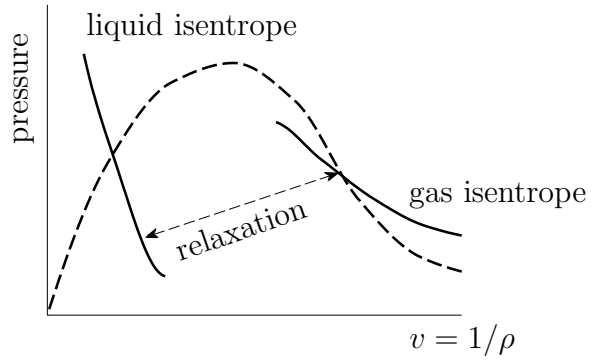

Figure 3: Liquid and gas isentropes are connected through a kinetic path (Gibbs free energy relaxation process) during phase change.

as a simplified VdW one, with a cure of the convexity issue. The main formulas for this EOS, named NASG (for Noble-Abel-Stiffened-Gas) read for a given phase $k = 1, 2$:

$$\begin{aligned} p_k(\rho_k, e_k) &= \frac{\rho_k(\gamma_k - 1)(e_k - q_k)}{(1 - \rho_k b_k)} - \gamma_k p_{\infty k}, \\ T_k(p_k, \rho_k) &= \frac{(p_k + p_{\infty k})(1 - \rho_k b_k)}{\rho_k C_{vk}(\gamma_k - 1)} \\ g_k(p_k, T_k) &= (\gamma_k C_{vk} - q'_k)T_k - C_{vk}T_k \ln \frac{T_k^{\gamma_k}}{(p_k + p_{\infty k})^{\gamma_k - 1}} + b_k p_k + q_k \end{aligned} \tag{6}$$

For a given phase, the following parameters are needed: γ_k, $p_{\infty k}$, b_k, C_{vk}, q_k, and q'_k. As shown in Le Metayer and Saurel (2015) there is no difficulty to determine these parameters once the saturation curves for the liquid and gas are known. For liquid water and steam the set of parameters in Tab. 1 has been determined in the temperature range [300 K, 500 K].

Expressing the thermal EOS of System (6) differently the following relation appears:

$$p_k(\rho_k, T_k) = \frac{\rho_k(\gamma_k - 1)C_{vk}T_k}{(1 - \rho_k b_k)} - p_{\infty k}. \tag{7}$$

Coefficients	Liquid phase	Vapor phase
$C_P(J/kg/K)$	4285	1401
$C_v(J/kg/K)$	3610	955
γ	1.19	1.47
$P_\infty(Pa)$	7028×10^5	0
$b(m^3/kg)$	6.61×10^{-4}	0
$q(J/kg)$	-1177788	2077616
$q'(J/(kg.K))$	0	14317

Table 1: 'NASG' coefficients for water and steam determined for $T \in [300 - 500\ K]$

The agitation part is $\rho_k(\gamma_k - 1)C_{vk}T_k$ and is similar to the ρRT part of (5). The repulsive part is the same in both VdW and NASG EOSs. The attractive part , $-p_{\infty k}$, is here a constant while it is density varying with the VdW EOS. The sound speed of a given phase reads,

$$c_k = \sqrt{\gamma_k \frac{p_k + p_{\infty k}}{\rho_k(1 - \rho_k b_k)}}. \tag{8}$$

With this formulation the phases sound speed are always defined as the densities cannot reach excessive levels, since the pressures tend to infinity before the densities reach their upper bounds. The constants q_k and q'_k represent respectively the internal energy and entropy constants, similar to energy and entropy reference states. They are determined in order that the latent heat $L_v(T)$ and the saturation pressure $p_{sat}(T)$ compare well with their experimental values. The various experimental and computed saturation variables are presented in Figure 4 showing excellent agreement in the considered temperature range [300 K, 500 K] used to fit the various EOS parameters.

Having in hands EOS (6) for each phase we now address building of the EOS for the mixture.

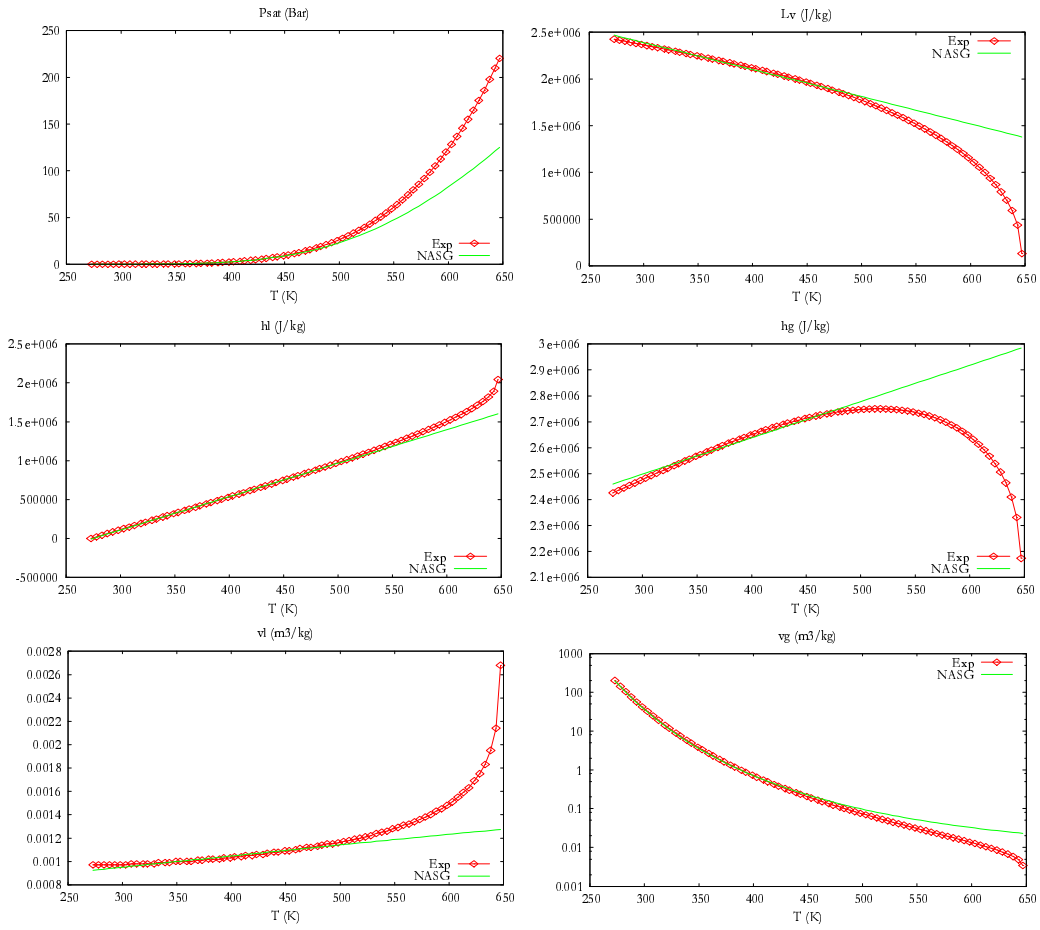

Figure 4: Comparison of the computed saturation curves with NASG formulations and experimental data in the temperature range [300 K, 500 K]. Excellent agreement is obtained in this range.

Mixture EOS

The mixture EOS is the one that closes System (1) with the help of mixture rules (2) on the basis of formulation (6) for each phase. The algebraic system to solve is thus,

$$\begin{aligned} e &= Y_1 e_1(T,p) + Y_2 e_2(T,p), \\ v &= Y_1 v_1(T,p) + Y_2 v_2(T,p), \end{aligned} \tag{9}$$

where e and v are obtained from the resolution of (1) and combination of the mass, momentum and energy equations. The unknowns in (9) are consequently the mixture temperature T and pressure P. Combining the caloric and thermal EOSs of (6) the energy for a given phase reads,

$$e_k(T_k, \rho_k) = C_{vk} T_k + (1/\rho_k - b_k) p_{\infty k} + q_k.$$

Inserting this expression in the first equation of (6) the specific volume as a function of pressure and temperature is obtained:

$$v_k(T_k, p_k) = \frac{(\gamma_k - 1) C_{vk} T_k}{p_k + p_{\infty k}} + b_k. \tag{10}$$

Inserting this expression in one of the EOS (6) the internal energy as a function of pressure and temperature is obtained:

$$e_k(T_k, p_k) = \frac{(p_k + \gamma_k p_{\infty k}) C_{vk} T_k}{p_k + p_{\infty k}} + q_k$$

With these definitions, System (9) becomes,

$$T(e, p, Y_1) = (e - \bar{q}) \left(\sum_i \frac{Y_i C_{vi} (p + \gamma_i p_{\infty i})}{p + p_{\infty i}} \right)^{-1}, \tag{11}$$

$$T(v, p, Y_1) = (v - \bar{b}) \left(\sum_i \frac{(\gamma_i - 1) Y_i C_{vi}}{p + p_{\infty i}} \right)^{-1}, \tag{12}$$

with the following definitions,

$$\begin{aligned} \bar{q} &= Y_1 q_1 + Y_2 q_2, \\ \bar{b} &= Y_1 b_1 + Y_2 b_2. \end{aligned}$$

Eliminating the temperature from these two equations the EOS for the pressure is obtained as solution of the following quadratic equation:

$$a_2 p^2 + a_1 p + a_0 = 0$$

$$\begin{aligned} a_2 &= Y_1 C_{v1} + Y_2 C_{v2} \\ a_1 &= Y_1 C_{v1}(p_{\infty_2} + \gamma_1 p_{\infty 1} - (\gamma_1 - 1)Q) + Y_2 C_{v2}(p_{\infty_1} + \gamma_2 p_{\infty 2} - (\gamma_2 - 2)Q) \\ a_0 &= -Q((\gamma_1 - 1)Y_1 C_{v1} p_{\infty 2} + (\gamma_2 - 1)Y_2 C_{v2} p_{\infty 1})) + p_{\infty 1} p_{\infty 2}(\gamma_1 Y_1 C_{v1} + \gamma_2 Y_2 C_{v2}) \end{aligned}$$

where

$$Q = \frac{e - \bar{q}}{v - \bar{b}}$$

The pressure is given by the only positive root:

$$p = \frac{-a_1 + \sqrt{a_1^2 - 4a_0 a_2}}{2a_2} \tag{13}$$

Once the pressure is determined, the temperature is computed by either (11) or (12). The mixture sound speed has a non-monotonic behaviour versus the volume fraction as shown in Figure 4.

From the results shown in Figure 5 it appears that there is no practical need to compute the mixture sound speed that is quite complex and computationally expensive (its explicit expression is given in Le Martelot *et al.* (2014)). As it is always lower than the mechanical equilibrium one, this one is preferred in the numerical computations, as better stability is guaranteed

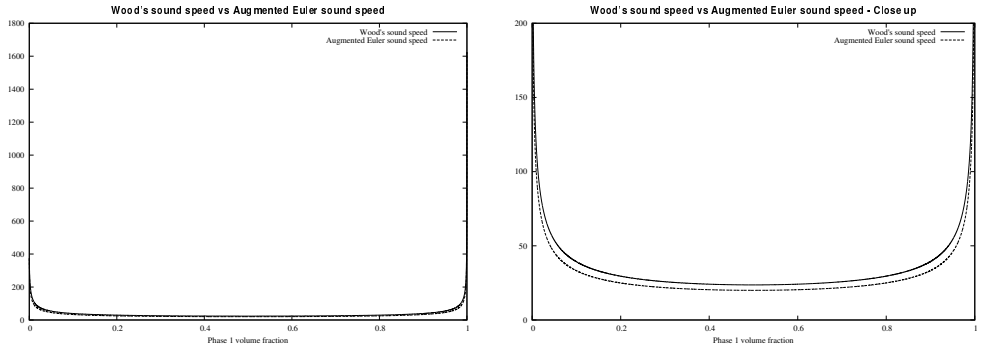

Figure 5: Representation of the mechanical equilibrium mixture sound speed (in lines) and the pressure-temperature equilibrium mixture sound speed (in dashed lines). Both sound speeds present a non-monotonic behaviour versus volume fraction. The mechanical equilibrium sound speed is always slightly higher than the pressure-temperature equilibrium one.

with this estimate. The mechanical equilibrium sound speed obeys the well known Wood (1930) formula:

$$\frac{1}{\rho c_w^2} = \frac{\alpha_1}{\rho_1 c_1^2} + \frac{\alpha_2}{\rho_2 c_2^2} \tag{14}$$

The volume fractions are determined from the resolution of System (1) and the specific volumes computed by (10) with the pressure given by (13) and temperature given by (12). The phase sound speeds are given by (8).

4. Kinetic relaxation rate - Thermo-chemical relaxation solver

When dealing with phase transition the relaxation rate ν present in the concentration equation (3) has to be specified. Following Saurel *et al.* (2008), the guess $\nu \to \infty$ is appropriate. In other words, pure liquid and pure gas are allowed to have any temperature, but instantly reach thermodynamic equilibrium at the saturation conditions where both liquid and gas are present (interface and mixture zones). This assertion is justified as follows:

– When dealing with the direct numerical simulation of boiling flows, the fluids become metastable as a consequence of heat diffusion. Heat conduction is slow and controls the global rate of phase change. Thus, one can assume that phase transition occurs at any rate, given it is greater than heat conduction. For the sake of simplicity, infinitely fast relaxation is adopted.

– When dealing with cavitating flows, it is assumed that the fluids contain enough impurities to have many nucleation sites. Around evaporating interfaces, phase transition happens and their collective effects result in macroscopic cavitation fronts surrounded by mushy zones. In these mushy zones the interfacial area is so large that heat and mass exchange are intense enough so that a flow model with a unique temperature and stiff Gibbs energy relaxation is appropriate.

– When none of the fluids is metastable (pure liquid state and pure gas state) no thermo-chemical relaxation occurs and the flow model reduces to single phase equations, with appropriate thermodynamics.

With this approach the thermodynamic path that the fluid follows during an isentropic expansion is shown in Fig. 2.

As the thermo-chemical solver is used as soon as metastable states appear, the effective thermodynamic path that the fluid follows is that of Fig. 2. Such a path could be reproduced by a reduced version of the flow model (1) with three equations only (mixture mass, mixture momentum and mixture energy), as in Downar-Zapolski *et al.* (1996) and Barret *et al.* (2002). However, the sound speed of such a model is not convenient, as it is costly to

compute, and most importantly, discontinuous at the phase diagram boundaries.

Here, the flow model has a sound speed always defined and continuous. As mentioned earlier, Eq. (14) is a fair approximation. Also, extending System (1) to the presence of non-condensable gas is straightforward while it is non-trivial with a more reduced model.

The presence of a stiff relaxation term in (3) does not result in computational difficulties as integration of such term is never addressed: in the following, only the equilibrium state is required. To compute the equilibrium state, a non-linear method is needed. It is worth mentioning however than in cavitating flows, a simplified method can be used as weak variations only of the temperature are present. Indeed, the flow is mainly made of liquid with high thermal inertia. Assuming the mixture temperature as constant, the equilibrium pressure can be estimated ($p = p_{sat}(T_m)$) and the liquid and gas concentrations deduced easily from (15) and (16). However, this method is not general when the liquid concentration is arbitrary.

The relaxed solution in the non-linear case corresponds to thermodynamic equilibrium, and is obtained considering the mixture mass and mixture energy definition :

$$v = \frac{1}{\rho} = Y_1 v_1 + Y_2 v_2 = cst = v_0 \quad (15)$$

$$e = Y_1 e_1 + Y_2 e_2 = cst = e_0 \quad (16)$$

where $Y_1 = \dfrac{\alpha_1 \rho_1}{\rho}$ and $Y_2 = \dfrac{\alpha_2 \rho_2}{\rho} = 1 - Y_1$ are the varying mass fractions of both phases. In the following the liquid and its vapor are denoted respectively by the subscripts '1' and '2'.

The specific volumes and internal energies are given by 'NASG' EOS relations:

$$v_k = \frac{(\gamma_k - 1)C_{vk}T_k}{p_k + p_{\infty,k}} + b_k, \tag{17}$$

$$e_k = C_{vk}T_k\left(1 + \frac{(\gamma_k - 1)p_{\infty,k}}{p_k + p_{\infty,k}}\right) + q_k, \tag{18}$$

All parameters appearing in relations (17), (18) and(19) are computed in order to satisfy the experimental liquid/vapor saturation curves (Le Métayer and Saurel 2015).

The final relaxed state, denoted by the superscript '$*$' corresponds to the thermodynamic equilibrium state. The liquid and vapor phases have a common pressure, temperature and Gibbs free energy. Equality of Gibbs free energy of both phases,

$$g_k = h_k - T_k s_k = (\gamma_k C_{vk} - q'_k)T_k - C_{vk}T_k ln\frac{T_k^{\gamma_k}}{(p + p_{\infty,k})^{\gamma_k - 1}} + b_k P_k + q_k, \tag{19}$$

provides a relation between the pressure and the temperature :

$$T^*(p^*) = T_{sat}(p^*) \tag{20}$$

This relation represents the evolution of the saturation temperature as a function of pressure. Thanks to (20), the relation (15) reads,

$$v_0 = Y_1^* v_1^*(p^*) + Y_2^* v_2^*(p^*) = Y_1^* v_1^*(p^*) + (1 - Y_1^*)v_2^*(p^*), \tag{21}$$

with,

$$v_k^*(p^*) = \frac{(\gamma_k - 1)C_{vk}T^*(p^*)}{p^* + p_{\infty,k}} + b_k. \tag{22}$$

Variables v_1^* and v_2^* thus correspond to the saturated specific volumes of the liquid and vapor phases respectively.

A first relation linking the liquid mass fraction and the pressure is obtained from (21) :

$$Y_1^* = \frac{v_2^*(p^*) - v_0}{v_2^*(p^*) - v_1^*(p^*)} \tag{23}$$

In relation (23) the existence of physical solution is fulfilled by the following condition :

$$0 < Y_1^* < 1 \Leftrightarrow v_1^*(p^*) < v_0 < v_2^*(p^*) \tag{24}$$

By using once more the saturation relation (20), the total energy equation (16) becomes

$$e_0 = Y_1^* e_1^*(p^*) + Y_2^* e_2^*(p^*) = Y_1^* e_1^*(p^*) + (1 - Y_1^*) e_2^*(p^*) \tag{25}$$

where

$$e_k^*(p^*) = C_{vk} T^*(p^*) \left(1 + \frac{(\gamma_k - 1) p_{\infty,k}}{p^* + p_{\infty,k}}\right) + q_k \tag{26}$$

A second relation linking the liquid mass fraction and the final pressure is obtained

$$Y_1^* = \frac{e_0 - e_2^*(p^*)}{e_1^*(p^*) - e_2^*(p^*)}. \tag{27}$$

It is more convenient to rewrite relation (27) in terms of specific enthalpies by combining (21) and (25),

$$e_0 + p^* v_0 = Y_1^* \left(e_1^*(p^*) + p^* v_1^*(p^*)\right) + Y_2^* \left(e_2^*(p^*) + p^* v_2^*(p^*)\right) = Y_1^* h_1^*(p^*) + Y_2^* h_2^*(p^*), \tag{28}$$

which directly introduces the latent heat of vaporization $L_v(p^*)$,

$$L_v(p^*) = h_2^*(p^*) - h_1^*(p^*). \tag{29}$$

Equation (27) then becomes :

$$Y_1^* = \frac{h_2^*(p^*) - (e_0 + p^* v_0)}{h_2^*(p^*) - h_1^*(p^*)} \tag{30}$$

In relation (30) a second existence condition appears :

$$0 < Y_1^* < 1 \Leftrightarrow h_1^*(p^*) < e_0 + p^* v_0 < h_2^*(p^*) \tag{31}$$

Equating relations (23) and (30) leads to an equation where the final pressure p^* is the only unknown :

$$\frac{h_2^*(p^*) - (e_0 + p^* v_0)}{h_2^*(p^*) - h_1^*(p^*)} - \frac{v_2^*(p^*) - v_0}{v_2^*(p^*) - v_1^*(p^*)} = 0 \tag{32}$$

Once the solution of (32) is obtained – through Newton's method for instance – the other thermodynamic variables are easily obtained by the preceding relations presented above.

However equation (32) may not provide a physical solution depending on the initial energy e_0 and specific volume v_0. This is the case when conditions (24) and (31) are not fulfilled. Then the liquid/vapor system tends towards a final state where a single phase is present. Total evaporation or condensation thus occurs during the relaxation process, and the corresponding thermodynamic state is computed with Eq. (13).

5. Hyperbolic solver

For the sake of simplicity, the presentation of the solver is one-dimensional, and limited to first order. Details about higher order extensions can be found in Toro (2009)

System (1) can be written in compact form as,

$$\frac{\partial U}{\partial t} + \frac{\partial F(U)}{\partial x} = 0, \tag{33}$$

where $U = \begin{bmatrix} \rho & \rho u & \rho E & \rho Y \end{bmatrix}^t$ are the conservative variables, and $F = \begin{bmatrix} \rho u & \rho u^2 + p & (\rho E + p)u & \rho u Y \end{bmatrix}^t$ are the associated fluxes.

Godunov Scheme

System (33) is a hyperbolic set of conservation laws, with wave speeds u, $u - c_{eq}$ and $u + c_{eq}$. The first-order Godunov method reads,

$$U_i^{n+1} = U_i^n - \frac{\Delta t}{\Delta x}(F^*_{i+1/2} - F^*_{i-1/2}), \tag{34}$$

under the CFL stability condition,

$$\Delta t \leq \frac{\Delta x}{\max(u \pm c_{eq})}. \tag{35}$$

The cell boundary fluxes $F_{i\pm1/2}$ are computed from the following approximate solver.

HLLC solver

The HLLC solver (Toro *et al.* 1994) is an approximate Riemann solver for the Euler equations that is easy to adapt to the present "real gas" context. In this frame, each wave is considered as a discontinuity :

- a contact discontinuity wave, with characteristic speed S_M (medium wave), through which pressure and velocity is constant,
- two shock waves, with characteristic speed S_L and S_R (left and right waves), through which mass fractions Y_i are constant.

As shown in Fig 6, each of these waves separate states $(\bar{U}_L, \bar{U}^*_L, \bar{U}^*_R, \bar{U}_R)$, from which it is possible to compute the appropriate flux between the two cells during the time-step.

In the example depicted in Fig. 6, U^*_L is the appropriate state to compute the intercell flux F, since it is the state which will persist at the physical

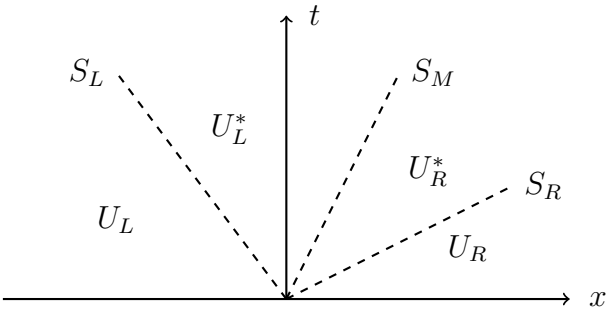

Figure 6: Schematic representation of the Riemann problem emerging at each cell boundary. Three non-linear waves are emitted, each one being considered as a discontinuity.

position of the cell discontinuity during the time step. In a more general context, there are four possible cases depending on the signs of the three wave velocities:

case a $S_L > 0 \rightarrow F = F(U_L)$

case b $S_R < 0 \rightarrow F = F(F_R)$

case c $S_M > 0, S_L < 0 \rightarrow F = F(U_L^*)$

case d $S_M < 0, S_R > 0 \rightarrow F = F(U_R^*)$

Wave speeds and fluxes estimates

Following Davis (1988), the right and left waves velocities can be approximated as,

$$S_R = \max((u+c)_R, (u+c)_L), \tag{36}$$

$$S_L = \min((u-c)_R, (u-c)_L). \tag{37}$$

Let us mention that other wave speed estimated are possible. Denoting S^+ a positive wave speed, it is possible to define $S_R = S^+$ and $S_L = -S^+$. The

Rusanov wave speed estimate for S^+ is given by

$$S^+ = \max(|u_L - c_L|, |u_R - c_R|, |u_L + c_L|, |u_R + c_R|). \tag{38}$$

This estimate is very robust and is often used in high speed cavitating flow computations. Yet another robust wave speed estimate is given by Toro Toro (2009):

$$S^+ = \max(|u_L| + c_L, |u_R| + c_R). \tag{39}$$

Knowledge of c_{eq} is not required as it can be replaced everywhere by its approximation c_w in the solver that follows.

Each discontinuity obeys the Rankine-Hugoniot conditions given by:

$$[F] - S_k[U] = 0 \tag{40}$$

where S_k denotes the speed of the k^{th} discontinuity and [...] denotes the jump of a given variable across the discontinuity.

Under HLL approximation, the intermediate wave speed is given by

$$S_M = u^* = \frac{p_R - p_L + \rho_R u_R(u_R - S_R) - \rho_L u_L(u_L - S_L)}{\rho_R(u_R - S_R) - \rho_L(u_L - S_L)} \tag{41}$$

Using again the Rankine-Hugoniot jump conditions, one can derive the following relations for the intermediate state:

$$\begin{cases} \rho_R^* = \rho_R \frac{u_R - S_R}{S_M - S_R} \\ u_R^* = u^* = S_M \\ p_R^* = p_R + \rho_R(u_R - S_R)(u_R - S_M) \\ E_R^* = E_R + \frac{p_R(u_R - S_M)}{\rho_R(u_R - S_R)} - S_M(u_R - S_M) \\ Y_{R,i}^* = Y_{R,i} \qquad \text{(constant mass fraction through shock waves)} \end{cases} \tag{42}$$

These relations fully define the intercell set of conservative variables U_R^*, and consequently the flux $F(U_R^*)$ given by

$$F_R^* = F_R - S_R(U_R - U_R^*). \tag{43}$$

Substituting the L index to the R index in the above formula leads to a similar expression for the remaining flux $F(U_L^*)$.

The computational examples that follow were achieved with the DALPHADT code based on tetrahedron meshes. In this frame, the Godunov method reads,

$$U_{k,i}^{n+1} = U_{k,i}^{n+1} - \frac{\Delta t}{V_i} \sum_{f=1}^{4} (F_k^* . \vec{\eta})_f S_f, \tag{44}$$

where S_f is the face area, and $(F_k^* . \vec{\eta})_f$ represents the flux solution of the Riemann problem solved along the face normal vector $\vec{\eta}_f$ of a given face of the tetrahedron, as illustrated in Fig. 7.

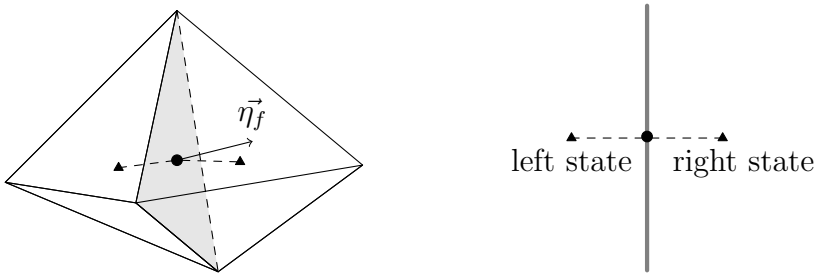

Figure 7: 3D Godunov method applied to tetrahedron meshes. The code is cell-centered, and the Riemann problem is resolved at each face. ▲ tetrahedron center. • face center.

We now address computational examples.

6. Cavitating flows

In this section, 2D two-phase flow computations in Venturi nozzle are addressed. The configuration studied corresponds to the experimental facility

built at LEGI Laboratory in Grenoble, France by the group leaded by S. Barre. The test section corresponds to a Venturi channel with a nozzle divergent inclined at an angle of 8° . The geometry is shown in Fig. 8.

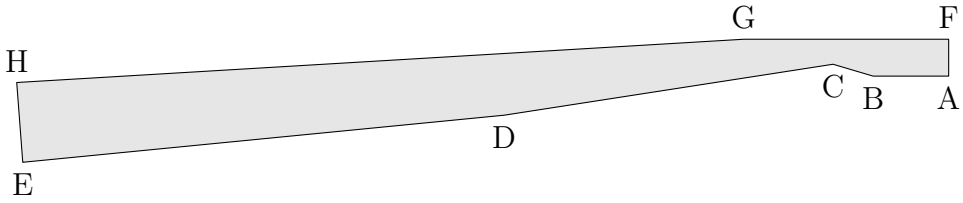

	X (abscissa) (m)	Y (m)		X(abscissa) (m)	Y (m)
A	0	0	E	1.225	-0.114
B	0.1	0	F	0	0.0488
C	0.153	0.0157	G	0.271	0.0488
D	0.588	-0.0517	H	1.233	-0.00845

Figure 8: Geometrical data of the Venturi 8° nozzle of LEGI, France.

The fluids considered correspond to liquid water and water vapor, with the NASG EOS and parameters given in Table 1. The boundary conditions correspond to imposed mass inflow with imposed stagnation enthalpy at the inlet and prescribed pressure at the outlet. The imposed conditions at the left inlet are the following,

$$\begin{cases} m = 7514.917\, kg.m^{-2}.s^{-1} \\ \rho_{liq} = 1067.56\, kg.m^{-3} \\ \rho_{vap} = 0.387\, kg.m^{-3} \\ \alpha_{liq} = 0.999 \\ P = 51825\, Pa \end{cases}$$

while, at the right outlet, the prescribed pressure is $P = 72025 Pa$.
With these boundary conditions a periodic flow has been observed experi-

mentally as shown in the Figure 9.

In the first stage of the cycle (a), a cavitation sheet is attached to the throat

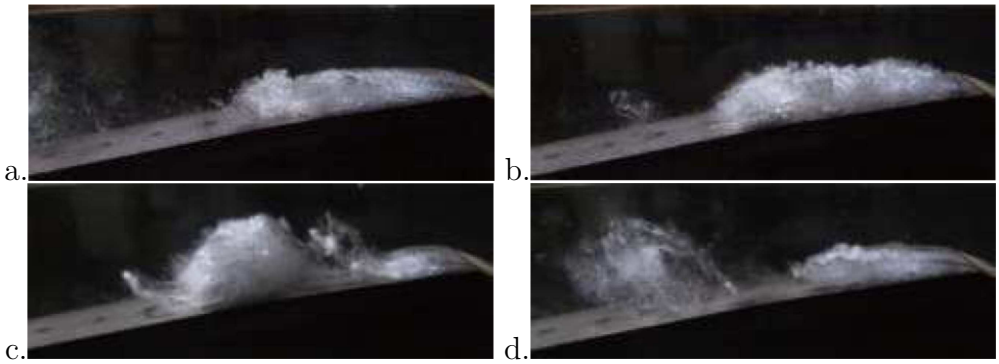

Figure 9: Experimental photographs of the break off cycle observed in the 8° Venturi nozzle with the boundary conditions aforementioned. A cavitation pocket appears, extends and separates in two sub-pockets, one transported with the mean flow and another one collapsing close to the nozzle. Courtesy of S. Barre.

and grows. In a second stage, the sheet reaches its maximum length (b) and breaks into two main parts (c). At the end, the downstream part is swept along within the stream and starts to collapse while the attached part starts another cycle (d). The mean attached cavity length value is 45 ± 5 mm while the quasi-periodic vapour cloud shedding frequency is about 45 Hz.
To compute this unstable flow a 2D unstructured mesh containing 52450 cells is used. The grid is refined at the throat in order to capture the cavitation pocket. The average cell size is 0.013 mm at throat and 0.08 mm elsewhere.

The explicit scheme summarized in Section 5 is extended to time implicit integration and the Riemann problem is preconditioned with the method detailed in Le Martelot *et al.* (2013). The flow is computed during 1.8 s of physical time, this time being long enough to obtain a quasi-stationary flow with quasi-periodic vapour clouds shedding. An example of the obtained

cloud shedding is shown in the volume fraction contours of Figure 10. Ex-

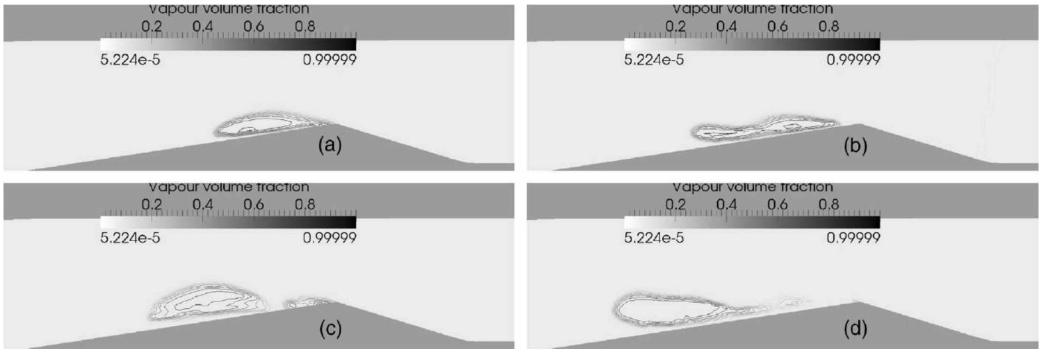

Figure 10: Computed volume fraction of water vapour. This example shows the same four stages as those observed during the experimental studies and shown in Figure 9. The mean attached cavity length is about 45mm, in perfect agreement with the experiments.

amining the water vapor volume fraction contours oscillations, we were able to determine a vapor pocket shedding frequency of about 43Hz, in excellent agreement with the measured frequency for the pressure fluctuations (45 Hz.).

By performing measurements during every cycle, an average attached cavity length of about 45 mm has been measured from the computations. These results show very good agreement with the experiments. Indeed, experimental measurements gave a mean attached cavity length equals to 45 $\pm$ 5 mm.

These results show that it is possible to reproduce the large structures of such cavitating flows with a flow model free of parameters. In particular, no turbulence model is used.

7. Evaporating flows

In this section, the capabilities of the flow model are illustrated in an evaporating liquid jet configuration, a configuration reminiscent of coaxial

liquid jet, in conditions typical of rocket engine at ignition. The flow under study contains liquid oxygen and gaseous oxygen at cryogenic temperatures. The 'NASG' parameters for oxygen are given below.

Coefficients	Liquid phase	Vapor phase
$C_P(J/kg/K)$	1741	552
$C_v(J/kg/K)$	791	299
γ	2.2	1.85
$P_\infty(bar)$	2036	0
$b(m^3/kg)$	4.57×10^{-4}	0
$q(J/kg)$	-290222	29274
$q'(J/(kg.K))$	0	-7527

Table 2: 'NASG' coefficients for oxygen determined for $T \in [80 - 120\ K]$
blue

The 3D computation is carried out in a rectangular parallelepiped of size $(3d \times 3d \times 8d)$. The outlet $(3d \times 3d)$ is a square area where atmospheric pressure is imposed through a non-reflecting boundary condition. The inlet $(3d \times 3d)$ is separated in two regions delimited by a circle of diameter $d = 5$mm at its center. In both regions, a mass flow rate is imposed through a non-reflecting conditions, with conditions:

- central flow: pure liquid oxygen, at 89K and 10m/s.
- peripheral flow: pure gaseous oxygen, at 200K and 100m/s.
- ambient pressure: 1atm.

The remaining four walls are symmetric boundary conditions.

The small scale destabilization of the liquid jet requires to extend the numerical solver presented in section 5 to higher order. This was achieved following the MUSCL-Hancock scheme with Superbee limiter.

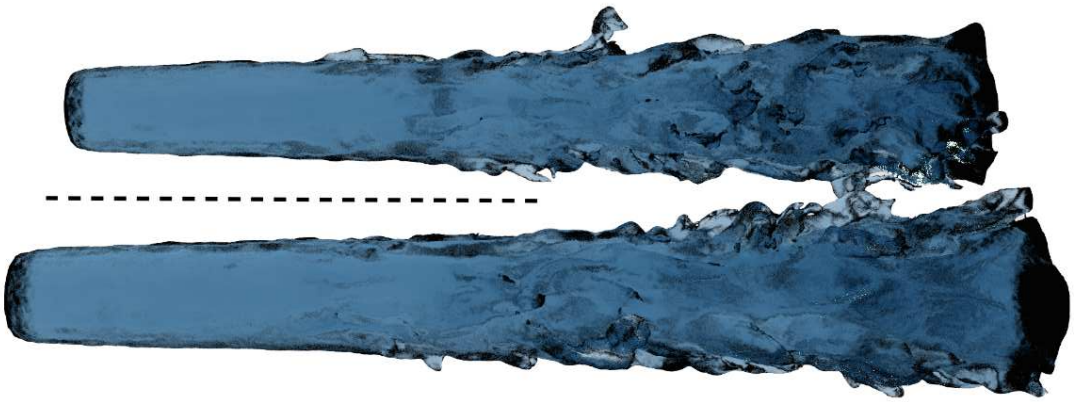

Figure 11: Iso-surface $Y_l = 0.5$, in the 3D computation of a liquid oxygen jet. The dashed-line indicates the symmetry condition in the 3D computations, and the jet is mirrored accordingly in the visualization.

In a first 3D computation of the configuration, ran on a 7 million cell unstructured mesh, the resolution of the flow model was carried out without the thermochemical relaxation solver (ie. without evaporation model). An iso-surface of the resulting jet, at $Y_l = 0.5$, is shown in Fig. 11. The results are very promising in that no inbound forcing was required to destabilize the liquid jet, and therefore prove the ability of the flow model to this challenging test case.

Two additional simulations have been carried out with a similar spatial discretization but in 2D, with the aim of studying the effect of evaporation

through the thermochemical relaxation solver on the jet destabilization. The contours of liquid oxygen mass fraction as obtained with and without evaporation effects are compared in Fig. 12. The simulated jet expectingly seems

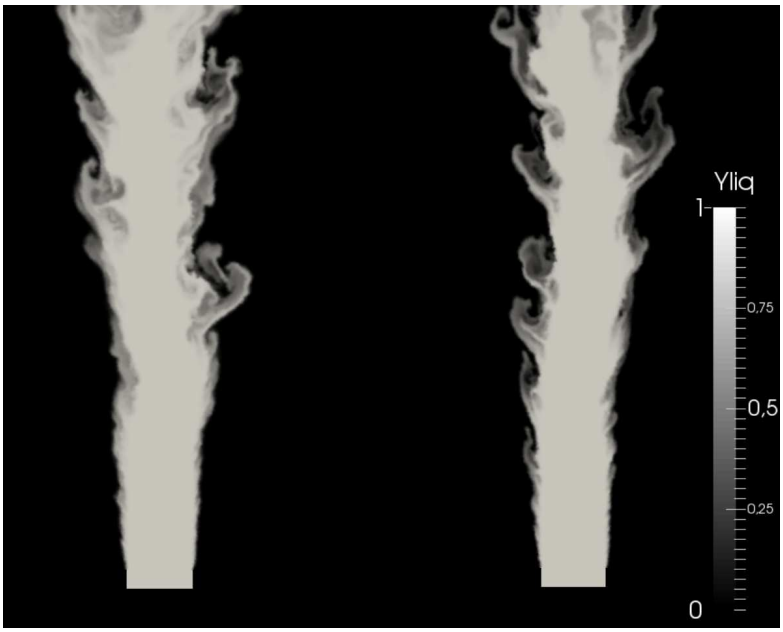

Figure 12: Liquid mass fraction fraction contour in a liquid oxygen – gaseous oxygen coaxial jet, at atmospheric pressure. The 2D simulations have been carried out without (left) and with (right) evaporation.

more destabilized because of the 2D confinement, but the result of interest is the effect of evaporation on such a jet. The filaments separating from the main liquid core are progressively evaporated due to the heat-transfer from the gaseous oxygen (at 200K), and the liquid oxygen (at 89K), modifying the flow.

In future works, the thermochemical relaxation solver will be extended, to account for the multiphase gas mixture (H_2, He, H_2O, etc.) which is present in the envisioned application. Capillary effects are not included in these sim-

ulations, because the intense velocity gradients make them negligible in the present jet destabilization conditions. Also, capillary effects are responsible for the filament size and their breakup that results in small drops. However, comparing the results of the two pictures in Fig. 12, it appears that small fragments are removed by phase change.

However, capillary effects may be of importance when the filaments start separating from the jet, and our future work will include them, following the strategy presented in the next section.

8. Boiling flows

To deal with DNS-type of boiling flows, System (1) has to be enhanced by introducing additional physical effects:

– buoyancy,

– surface tension,

– heat conduction.

Surface tension effects are considered through the Continuum Surface Force (CSF) method of Brackbill *et al.* (1992). The capillary force is modelled as,

$$\mathbf{F}_\sigma = \sigma\kappa\overrightarrow{\nabla Y_1} \tag{45}$$

where σ represents the surface tension coefficient ($N.m^{-1}$), κ represents the local curvature (m^{-1}) and Y_1 is the mass fraction of phase 1. The local curvature reads,

$$\kappa = -div\left(\frac{\overrightarrow{\nabla Y}}{|\overrightarrow{\nabla Y}|}\right). \tag{46}$$

The gravity force is modelled as,

$$\mathbf{F}_g = \rho \mathbf{g},$$

where $\mathbf{g}$ represents the gravity constant.

Heat conduction is inserted in the total energy equation of the model through the Fourier law $\mathbf{q} = -\lambda_c \overrightarrow{\nabla T}$ where the "mixture" thermal conductivity is given by $\lambda_c = \alpha_1 \lambda_1 + \alpha_2 \lambda_2$ and λ_k represents the thermal conductivity of phase k. Details are given in Le Martelot et al. (2014).
Inserting these extra effects, the flow model now becomes:

$$\begin{aligned}
&\frac{\partial \rho Y_1}{\partial t} + div\left(\rho Y_1 \mathbf{u}\right) = \rho \nu (g_2 - g_1) \\
&\frac{\partial \rho}{\partial t} + div\left(\rho \mathbf{u}\right) = 0 \\
&\frac{\partial \rho \mathbf{u}}{\partial t} + div\left(\rho \mathbf{u} \otimes \mathbf{u} + P \underline{\underline{I}}\right) = \sigma \kappa \overrightarrow{\nabla Y_1} + \rho \mathbf{g} \\
&\frac{\partial \rho E}{\partial t} + div\left((\rho E + P)\mathbf{u}\right) = div\left(\lambda_c \overrightarrow{\nabla T}\right) + \sigma \kappa \overrightarrow{\nabla Y_1} \bullet \mathbf{u} + \rho \mathbf{g} \bullet \mathbf{u}
\end{aligned} \tag{47}$$

A conservative form is available as well,

$$\begin{aligned}
&\frac{\partial \rho Y_1}{\partial t} + div\left(\rho Y_1 \mathbf{u}\right) = \rho \nu (g_2 - g_1) \\
&\frac{\partial \rho}{\partial t} + div\left(\rho \mathbf{u}\right) = 0 \\
&\frac{\partial \rho \mathbf{u}}{\partial t} + div\left(\rho \mathbf{u} \otimes \mathbf{u} + P \underline{\underline{I}} - \sigma \underline{\underline{\mathbf{m}}}\right) = \rho \mathbf{g} \\
&\frac{\partial \rho E + \sigma |\overrightarrow{\nabla Y_1}|}{\partial t} + div\left((\rho E + P + \sigma |\overrightarrow{\nabla Y_1}|)\mathbf{u} - \sigma \underline{\underline{\mathbf{m}}} \bullet \mathbf{u} - \lambda_c \overrightarrow{\nabla T}\right) = \rho \mathbf{g} \bullet \mathbf{u}
\end{aligned} \tag{48}$$

where $\underline{\underline{\mathbf{m}}} = \left(|\overrightarrow{\nabla Y_1}| \underline{\underline{I}} - \frac{\overrightarrow{\nabla Y_1} \otimes \overrightarrow{\nabla Y_1}}{|\overrightarrow{\nabla Y_1}|} \right)$.

This system is closed by the EOS (13). The entropy equation associated to System (47) reads,

$$\frac{\partial \rho S}{\partial t} + div\left(\rho S\mathbf{u} - \frac{\lambda_c \overrightarrow{\nabla T}}{T}\right) = \frac{\rho\nu(g_2 - g_1)^2}{T} + \lambda_c \frac{(\nabla T)^2}{T^2} \tag{49}$$

with $S = Y_1 s_1 + Y_2 s_2$, and shows agreement with the second law of thermodynamics.

System (48) is considered hereafter to compute boiling flow examples.

A closed and adiabatic rectangular domain (12cm x 7cm) in which the lower half is filled with saturated liquid water and the upper half is filled with saturated vapour is considered.

The surface tension coefficient is set to $\sigma = 73.10^{-3} N.m^{-1}$, the contact angle is taken constant and equal to $\theta = 45°$ and the gravity acceleration is set to $|\mathbf{g}| = 9.81\, m.s^{-2}$. The fluid parameters are the following:

Liquid water

$$\gamma_{liq} = 2.62 \quad P_{\infty,liq} = 9058.29\, 10^5\, Pa \quad C_{v,liq} = 1606.97\, J.kg^{-1}.K^{-1}$$

$$q_{liq} = -1.150975\, 10^6 J \quad \lambda_{liq} = 0.6788\, W.m^{-1}.K^{-1} \quad b_{liq} = 0\, m^3/kg$$

Water vapour

$$\gamma_{vap} = 1.38 \quad P_{\infty,vap} = 0\, Pa \quad C_{v,vap} = 1192.51\, J.kg^{-1}.K^{-1}$$

$$q_{vap} = 2.060759\, 10^6 J \quad \lambda_{vap} = 0.0249\, W.m^{-1}.K^{-1} \quad b_{vap} = 0\, m^3/kg$$

At start, the initial volume fraction of vapour is $\alpha_{vap} = 0.0001$ in the lower half domain and $\alpha_{vap} = 0.9999$ in the upper part. Moreover, the initial pressure and temperature are initialised with the hydrostatic gravity profile

with the constraint $T = T_{SAT}(P)$ in each cell. The bottom wall temperature is set constant at $T_{SAT}(P_{atm}) + 15K$.

The numerical scheme presented in the former section is rendered time implicit and the Riemann solver is low Mach pre-conditioned (Le Martelot et al., 2014). A mesh made of 960 x 560 cells is used in the computations that follow.

Three vapour bubbles (radius $= 3mm$) are set initially at the bottom wall as shown in the first image of Figure 13. The volume fraction of vapour inside these bubbles is $\alpha_{vap} = 0.9999$. The computed vapour mass fraction is shown in the same figure.

The first instants show the three first bubbles moving toward the surface due to buoyancy effects while, as the bottom wall of the box is heated, water around begins to boil, creating a vapour film. The boiling phenomenon appears as a consequence of wall heating effect that renders the liquid locally slightly overheated. Indeed, the assumption made is that the liquid contains enough impurities to not accept overheating, as pure liquids are able to become metastable while real liquids are not. Therefore, using the phase transition solver of Section 4 after checking that the liquid is not in stable state, the equilibrium state is computed on the basis of Eq. (32) and a mixed cell appears. From this "nucleation cell site" and merging effects due to surface tension, convection and inertia, new bubbles appear. Once created, theses new bubbles begin to rise and, as there is now again liquid in contact with the bottom wall, new bubbles appear behind them and begin to grow.

It is worth to mention that the bottom wall of the box is a perfect surface,

exempt of cavities or special treatment except for uniform temperature and constant contact angle. According to the velocity profiles, the first bubbles seem to be created between the convective rolls, where the velocity is the lowest, as shown in Figure 13.

9. Conclusions

Boiling, evaporation and cavitation are essentially the same phenomenon, driven by phase transition, but in different pressure and temperature conditions. Consequently, they ought to be described by the same model, and deriving such a model is the object of the present work. The flow model is essentially a hyperbolic system with relaxation terms. Coping with boiling, evaporation and cavitation, it is - in the authors knowledge - the first approach showing such a wide range of applicability. It is also a very robust computational approach of phase transition compared to existing alternatives. Although not shown here, our preliminary investigations show that the flow model can be extended to cope not only with a liquid-vapor couple, but also with multicomponent gas mixtures. This extension is the subject of an upcoming work.

Acknowledgements

Part of this work has been carried out in the framework of the Labex MEC (ANR-10-LABX-0092) and of the A*MIDEX project (ANR-11-IDEX-0001-02), funded by the Investissements d'Avenir French Government program managed by the French National Research Agency (ANR). We also acknowledge funding from ANR through project ANR-14-CE22-0014.

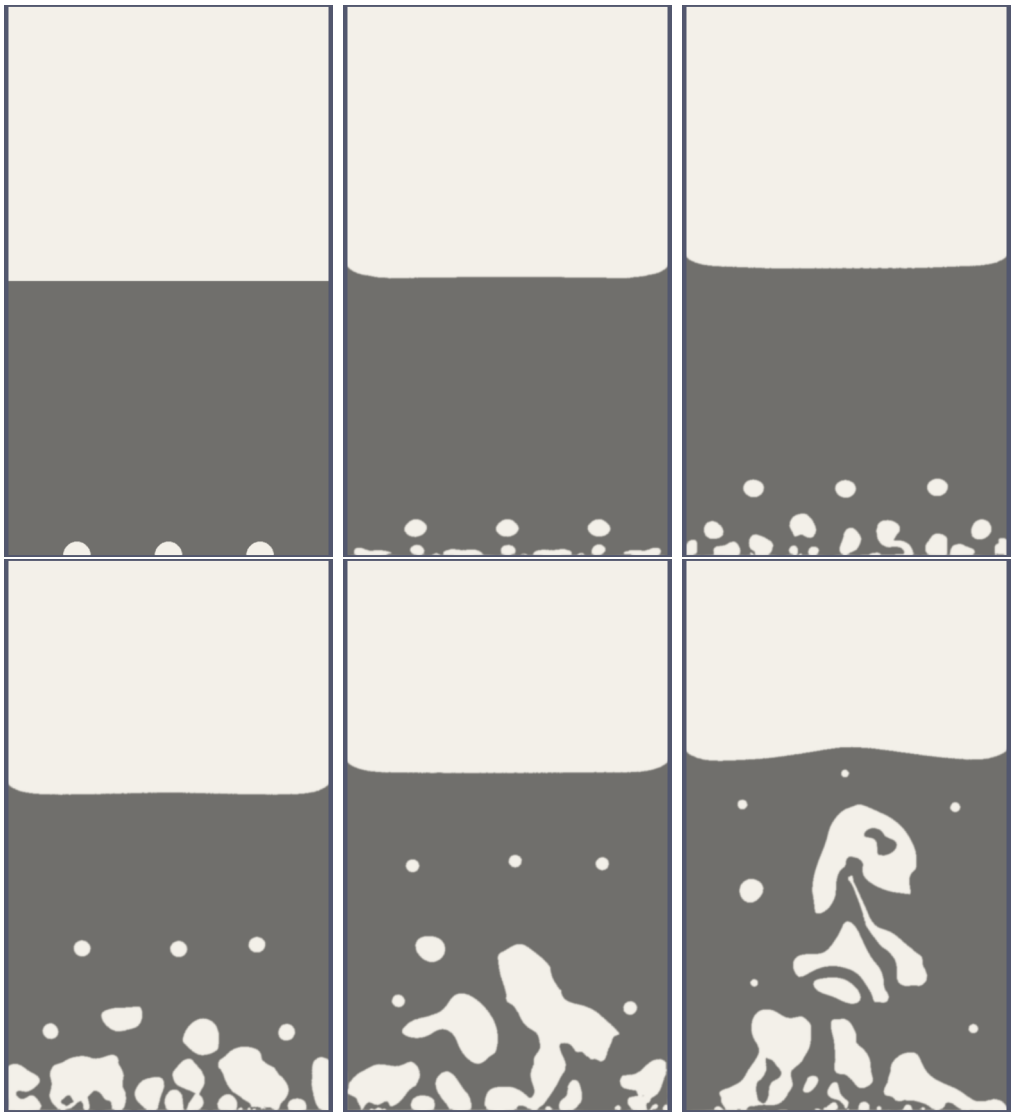

Figure 13: Vapour mass fraction contours at times $t = 0\,s$, $t = 50\,ms$, $t = 100\,ms$, $t = 200\,ms$, $t = 300\,ms$ and $t = 400\,ms$. The three first bubbles initially settled at the wall surface move up due to buoyancy, but as the wall is heated the water around them begins to evaporate and local vapour films appear. It forms new bubbles which rise as new ones appear behind.

References

Barre, S., Rolland, J., Boitel, G., Goncalves, E., and Patella, R.F., 2009. Experiments and modeling of cavitating flows in venturi: attached sheet cavitation, *European Journal of Mechanics-B/Fluids*, 28 (3), 444–464.

Barret, M., Faucher, E., Hé, J.M., and rard, 2002. Schemes to compute unsteady flashing flows, *AIAA journal*, 40 (5), 905–913.

Brackbill, J., Kothe, D.B., and Zemach, C., 1992. A continuum method for modeling surface tension, *Journal of computational physics*, 100 (2), 335–354.

Cahn, J.W. and Hilliard, J.E., 1958. Free energy of a nonuniform system. i. interfacial free energy, *The Journal of chemical physics*, 28 (2), 258–267.

Chaves, H., 1984. Changes of phase and waves on depressurization of liquids with high specific heat, *NASA STI/Recon Technical Report N*, 84, 25003.

Coutier-Delgosha, O., Fortes-Patella, R., and Reboud, J.L., 2003. Evaluation of the turbulence model influence on the numerical simulations of unsteady cavitation, *Journal of Fluids Engineering*, 125 (1), 38–45.

d'Agostino, L. and Salvetti, M.V., 2008. *Fluid dynamics of cavitation and cavitating turbopumps*, vol. 496, Springer Science & Business Media.

Davis, S., 1988. Simplified second-order godunov-type methods, *SIAM Journal on Scientific and Statistical Computing*, 9 (3), 445–473.

Downar-Zapolski, P., Bilicki, Z., Bolle, L., and Franco, J., 1996. The non-equilibrium relaxation model for one-dimensional flashing liquid flow, *International journal of multiphase flow*, 22 (3), 473–483.

Goncalves, E. and Patella, R.F., 2009. Numerical simulation of cavitating flows with homogeneous models, *Computers & Fluids*, 38 (9), 1682–1696.

Jamet, D., Lebaigue, O., Coutris, N., and Delhaye, J., 2001. The second gradient method for the direct numerical simulation of liquid–vapor flows with phase change, *Journal of Computational Physics*, 169 (2), 624–651.

Kapila, A., Menikoff, R., Bdzil, J., Son, S., and Stewart, D., 2001. Two-phase modeling of deflagration-to-detonation transition in granular materials: Reduced equations, *Physics of Fluids (1994-present)*, 13 (10), 3002–3024.

Le Martelot, S., Nkonga, B., and Saurel, R., 2013. Liquid and liquid–gas flows at all speeds, *Journal of Computational Physics*, 255, 53–82.

Le Martelot, S., Saurel, R., and Nkonga, B., 2014. Towards the direct numerical simulation of nucleate boiling flows, *International Journal of Multiphase Flow*, 66, 62–78.

Le Métayer, O., Massoni, J., and Saurel, R., 2004. Elaboration des lois d'état d'un liquide et de sa vapeur pour les modèles d'écoulements diphasiques, *International journal of thermal sciences*, 43 (3), 265–276.

Le Métayer, O. and Saurel, R., 2015. An alternative to cubic equations of state: The Noble-Abel - "Stiffened Gas" equation of state., submitted.

Lund, H., 2012. A hierarchy of relaxation models for two-phase flow, *SIAM Journal on Applied Mathematics*, 72 (6), 1713–1741.

Menikoff, R. and Plohr, B.J., 1989. The Riemann problem for fluid flow of real materials, *Reviews of modern physics*, 61 (1), 75.

Murrone, A. and Guillard, H., 2005. A five equation reduced model for compressible two phase flow problems, *Journal of Computational Physics*, 202 (2), 664–698.

Orbey, H. and Sandler, S.I., 1998. *Modeling vapor-liquid equilibria: cubic equations of state and their mixing rules*, vol. 1, Cambridge University Press.

Saurel, R., Cocchi, P., and Butler, P.B., 1999. Numerical study of cavitation in the wake of a hypervelocity underwater projectile, *Journal of Propulsion and power*, 15 (4), 513–522.

Saurel, R., Petitpas, F., Abgrall, R., *et al.*, 2008. Modelling phase transition in metastable liquids: application to cavitating and flashing flows, *Journal of Fluid Mechanics*, 607 (1), 313–350.

Simoes-Moreira, J.R. and Shepherd, J.E., 1999. Evaporation waves in superheated dodecane, *Journal of Fluid Mechanics*, 382, 63–86.

Sinibaldi, E., Beux, F., and Salvetti, M.V., 2006. A numerical method for 3D barotropic flows in turbomachinery, *Flow, turbulence and combustion*, 76 (4), 371–381.

Toro, E.F., 2009. *Riemann solvers and numerical methods for fluid dynamics: a practical introduction*, Springer Science & Business Media.

Toro, E.F., Spruce, M., and Speares, W., 1994. Restoration of the contact surface in the HLL-riemann solver, *Shock waves*, 4 (1), 25–34.

Wareing, C.J., Woolley, R.M., Fairweather, M., and Falle, S.A., 2013. A composite equation of state for the modeling of sonic carbon dioxide jets in carbon capture and storage scenarios, *AIChE Journal*, 59 (10), 3928–3942.

Wood, A., 1930. *A textbook of sound*, G. Bell and Sons Ltd., London.